# Chapter 8

# A Log-periodic Channelizer inspired by the Mammilian Cochlea

## 8.1  Introduction

Chapter 7 discussed the design and fabrication of diplexer and triplexer circuits with non-adjacent bands that can be used in terrestrial measurements. This chapter discusses a log-periodic channelizer inspired by the workings of the human ear. It has an arbitrary number of adjacent channels with an arbitrary total bandwidth. However, the filters' band centers are spaced log-periodically in frequency, making it difficult to position them between atmospheric lines. Instead, this channelizer is best suited for high-altitude applications.

We begin by discussing how the cochlea is similar to a transmission line and how it motivates a powerful channelizer design methodology. These first sections summarize prior efforts by our collaborators at UCSD to build circuits with lumped components. We then discus how the same components can be realized with printed features in our millimeter wavelength circuits. Finally, we show measurements of a sinuous antenna coupled to TES

bolometers (shown in Figure 8.1) through a cochlear channelizer and compare those results against simulations.



Figure 8.1. The cochlea removes monotonically lower frequencies as an acoustic pulse travels deeper into the ear. The mechanical resonant frequency of each section is related to it's neighbors by a geometric scaling factor. It is a biological example of a log-periodic structure. Cartoon taken from *Doe* [2010].

## 8.2   A cochlear channelizer

Channelizer circuits are similar to the filter manifolds discussed in the previous chapter, but have an arbitrary number of contiguous channels. Their synthesis has long been a major challenge to radio engineers. Most design methodologies use many components that must be constrained by extensive CAD (*Rauscher* [1994]) or they isolate filters with numerous hybrids that each have a very large foot-print (*Matthaei et al.* [1980]). However, in recent years, a community of radio-engineers have started using the physiology of the human ear as an inspiration for channelizers that are compact and require minimal CAD optimization (*Sarpeshkar et al.* [2007], *Galbraith* [2008], and *Watts* [1993]). Many of these approaches utilize active feedback, but our collaborators at UCSD have developed a methodology that

is entirely passive with just reactive components, making the designs realizable at cryogenic temperatures.

In most mammals, the cochlea converts acoustic energy into mechanical motion before triggering electrical signals within nerves. In the simplest models, the cochlea couples acoustic waves onto a basilar membrane whose local mechanical resonant frequency decreases *geometrically* with distance as the waves propagate (see the cartoon in Figure 8.2). When the sections resonate, they absorb and dissipate a narrow frequency range of acoustic waves, exciting signals within local nerve cells. The ear is channelizer that removes the highest frequencies first and lower frequencies later with each section's frequency related to it's neighbors by a geometric scaling factor. Because of this structure, the ear is log-periodic in an analogous way to the antennas discussed in chapter 5. The human ear covers nearly three octaves and can differentiate tones that fractionally differ in frequency by only 0.5%, corresponding to over 1000 contiguous channels! (*Galbraith et al.* [2008])
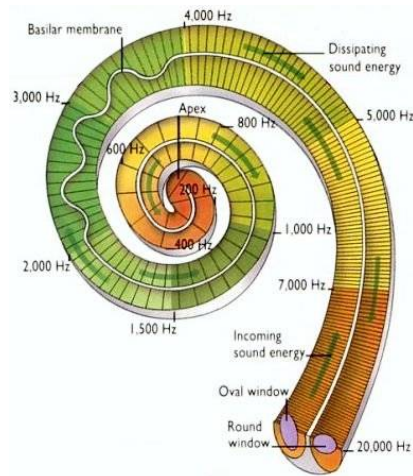


Figure 8.2. The entire log-periodic pixel. Each polarization of the sinuous couples to TES bolometers (at bottom)through separate cochlear channelizers. The antenna is roughly 1.2mm in diameter. Figure from *Doe* [2010]

The wave equation for pressure in the ear has a dispersion relation that is a nontrivial function of several physiological parameters. However, electrical engineers realized that this equation is equivalent to the voltage wave equation in the relatively simple circuit shown in Figure 8.3. This model essentially says that the ear is similar to a transmission

line, except with resistively-loaded single-pole LC-resonators shunting to ground instead of the pure capacitance found in a standard line. The filters' have identical Q, but their resonant frequencies monotonically decrease from left to right, each related to it's neighbors' resonance through a geometric scaling factor.
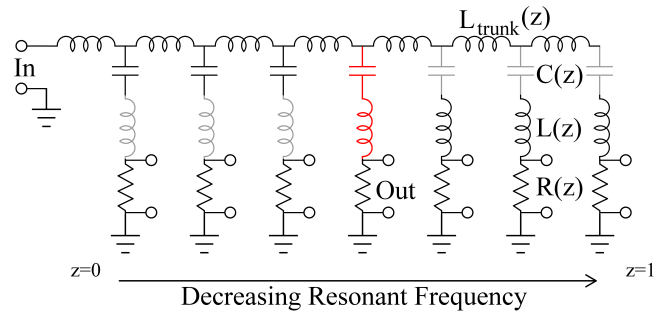


Figure 8.3. Single-pole channelizer

If a monochromatic wave enters the circuit in Figure 8.3 at the left with a frequency that resonates at a filter in the middle of the manifold (shown in red), the filters it passes prior to dissipation will have a higher resonant frequency and provide non-zero reactance that isolates the wave from ground. Their impedance will look approximately capacitive, and the manifold closely resembles a transmission line. We have drawn the capacitors at left in Figure 8.3 in gray to illustrate this effect. Most of that wave will dissipate in the red filter; the power that leaks through will see lower frequency filters that look like shunt inductors and will reflect the leaked wave back towards the correct filter. In contrast to most filter manifolds (including the diplexers and triplexers), this design does not seek to isolate filters; rather, it intentionally exploits each filters' non-resonant impedance.

Constructing the wave equation for an ideal transmission line is standard fare for most introductory electronics textbooks (e.g. *Pozar* [2004]) and we do not explicitly reproduce that here. To summarize, the wave equation results from the following procedure:

1. Calculate the voltage and current drops across each section from the Kirchoff circuit-junction rules.

2. Convert these to differential equations in the limit where the length of each section $\Delta z \to 0$.

3. Combine the two equations into one second order equation, typically for voltage.

This same procedure applies to the Circuit in Figure 8.3, except that we must generalize $1/j\omega C$ in the equation for current to $1/\left(1/j\omega C(z) + j\omega L(z) + R(z)\right)$. These components are a function of the distance $z$ from the input port, but they change slowly so the changes in series inductance $L_{\text{trunk}}(z)$ can be neglected when differentiating the voltage equation. The result of this analysis is a Voltage wave equation

$$\frac{d^2 V(z)}{dz^2} + \frac{L_{\text{trunk}}(z)C(z)}{1 + j\omega R(z)C(z) - \omega^2 L(z)C(z)}\omega^2 V(z) = 0 \tag{8.1}$$

where $z$ is defined between $z = 0$ at the input and $z = 1$ at the far right. This equation is identical in form to the pressure wave in the human ear, which means that the ear's structure can inform the decisions we make in choosing the components in each section. The ear's channels have constant fractional bandwidth (or $1/Q$), and physiological comparisons suggest that the dispersive terms must bear the following relationships:

$$L(z)C(z) = A_1 e^{\alpha z} \tag{8.2}$$

$$R(z)C(z) = A_2 e^{\alpha z/2} \tag{8.3}$$

$$L_{\text{trunk}}(z)C(z) = A_3 e^{\alpha z} \tag{8.4}$$

(*Galbraith et al.* [2008]). This realization reduces a circuit with potentially dozens of free parameters to four! In terms of these parameters, the passband center of each filter is simply

$$\omega_c = 2\pi f_c = \frac{1}{\sqrt{L_2(z)C(z)}} = \frac{e^{\alpha z/2}}{\sqrt{A_1}} \tag{8.5}$$

and the Q of each filter is:

$$Q = X/R = \sqrt{A_1}/A_2 \tag{8.6}$$

The end filters with pass-bands $f_N$ and $f_1$ correspond to $z = 0$ and $z = 1$. The choices of $Q, f_1$, and $f_N$ constrain three of these parameters:

$$A_1 = 1/(2\pi f_N)^2 \tag{8.7}$$

$$A_2 = \sqrt{A_1}/Q \tag{8.8}$$

$$\alpha = 2\log(f_N/f_1) \tag{8.9}$$

We can find the last parameter $A_3$ from a WKB solution of Equation 8.1 where we assume that the voltage wave's phase at each band center is an arbitrary constant, as suggested from physiological studies of the cochlea (*Galbraith et al.* [2008]). However, it is more practical to simply optimize this single free remaining parameter in CAD software.

## 8.3  Three-pole channelizer circuits

Most CMB cameras utilize filters that role off faster than single pole. Fortunately, the single-pole filters in Figure 8.3 can be replaced with higher-order ones provided that the filters have the correct limiting impedance. In particular, each filer's reactance still must be capacitive below it's pass-band and inductive above. While this is automatically satisfied by a single-pole filter, it is not always so for multi-pole filters. For example, the filter described in chapter 6 has off-resonance reactance that is opposite this, being *capacitive above* resonance and *inductive below*. Moreover, at frequencies far below resonance, the stubs in the filters short to ground. If implemented in a channelizer, the low frequency shorts would reflect nearly all incident power back towards the antenna. The shorted-stub filters are not appropriate for this application.
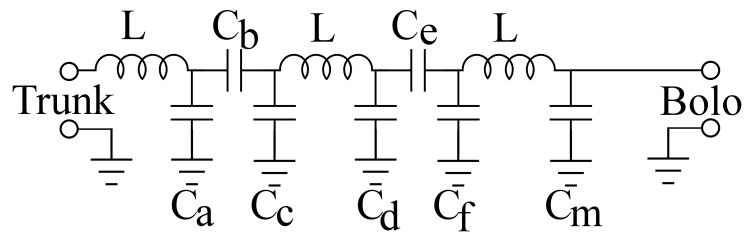
The Rebeiz group realized that filters like those in Figure 8.4(a) do have the required
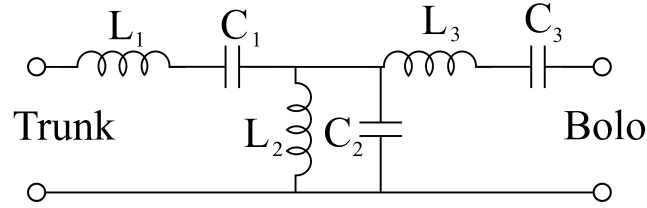
(a) Basic Filter
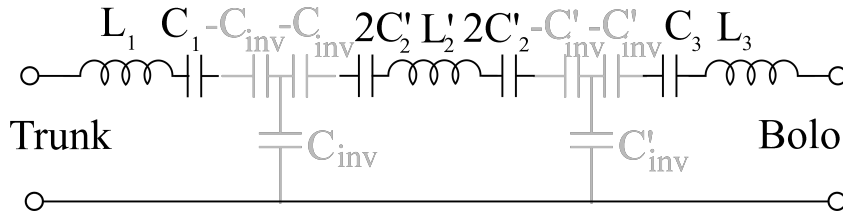


(b) Filter with Capacitive-T Inverters



(c) Tubular Filter

Figure 8.4. (a) An ideal 3-pole filter for the channelizer, (b) the same filter with the inner resonator inverted with a T-network, and (c) a tubular filter where pi-networks replace the T-networks.

limiting reactance (*Galbraith and Rebeiz* [2008]). This filter differs from those in Chapter 6 because each resonator has been inverted. Unfortunately, the lumped shunt inductance to ground is challenging to fabricate. To mitigate this difficulty, the Rebeiz group inverted the inner parallel resonator into a series one and surround it with a pair of capacitive T-networks with negative series capacitance (See Figure 8.4(b)). These networks are functionally similar to the $\lambda/4$ inverters in the filter described in Chapter 6, transforming a load impedance $Z_L$ into $X^2/Z_L$, where $X \equiv 1/\omega C_{inv}$ is the magnitude of the capacitors' reactance. In practice, the negative capacitors are simply absorbed into the resonators' smaller series caps. Other groups developing submillimeter channelizers have also used this filter (*Kumar* [2007]).

The required T-networks have large series and small shunt capacitors, which are difficult to fabricate in thin films in a way that ensures proper step-coverage over lower layers. However, converting these to pi-networks drastically decreases the series capacitors relative to the shunt capacitors, resulting in components that are easier to fabricate. This filter is known as a tubular filter (*Swanson* [1989]). We followed the lead of the Rebeiz group and chose the three series inductors to be identical within each filter and also included a matching shunt capacitor at the end to allow the filter's normalized input impedance to differ from the 10 $\Omega$ transmission line that terminates at the bolometers(*Pozar* [2004]).

The components in the these filter models are constrained entirely by (1) the pass-band center, (2) the filter bandwidth, and (3) the circuit impedance normalization. In practice, the filters' pass-bands are wider in the channelizer circuit than in isolation, so we cannot simply calculate this width from the relative band locations. Instead, we must numerically vary all three of these parameters as well as a normalization to the trunkline inductors $L_{\text{trunk}}(z) = L_o \exp(\alpha z/2)$ and an input shunt capacitor $C_{in}$ in order to minimize the reflection coefficient $S_1 1$ back to the antenna. We show the results of this optimization as well as the other components from Figure 8.4(c) in Tables 8.1 8.2.

Table 8.1.  Resonator Component Target Values

| Component | Admittance or Impedance |
|---|---|
| $L_{end}$ | $23.8m\mho$ |
| $L_{center}$ | $23.8m\mho$ |
| $\Pi_1, Y_{11}$ | $24.6m\mho$ |
| $\Pi_1, Y_{12}$ | $6.3m\mho$ |
| $\Pi_1, Y_{22}$ | $49.3m\mho$ |
| $\Pi_2, Y_{11}$ | $21.9m\mho$ |
| $\Pi_2, Y_{12}$ | $6.1m\mho$ |
| $\Pi_2, Y_{22}$ | $45.7m\mho$ |
| $C_{match}$ | $11.6\Omega$ |

Table 8.2. Trunkline Component Target Values

| Component | Inductance or Capacitance | Admittance |
|-----------|---------------------------|------------|
| $L_{222}$ | 1.88 pH | 381 $m\mho$ |
| $L_{184}$ | 2.11 pH | 410 $m\mho$ |
| $L_{152}$ | 2.37 pH | 442 $m\mho$ |
| $L_{126}$ | 2.65 pH | 477 $m\mho$ |
| $L_{104}$ | 2.97 pH | 515 $m\mho$ |
| $L_{86}$ | 3.33 pH | 556 $m\mho$ |
| $L_{71}$ | 3.73 pH | 601 $m\mho$ |
| $C_{in}$ | 69 fF | |

## 8.4 Millimeter-Wavelength channelizers

The Rebeiz group designed their circuits to work at microwave frequencies where it is possible to solder lumped components onto boards. Specifically, they soldered off-the-shelf series inductors and series capacitors into their circuits. This is neither possible nor practical for large arrays of millimeter-wavelength devices; *all* components must be printed in thin films. Figure 8.5 shows one of our printed tubular filters with a circuit diagram above. The capacitive pi-networks are MIM parallel-plate components, the resonator inductors are short high-impedance co-planar waveguide, and the trunk-line inductors are short microstrip lines. In this section, we discuss how we designed and fabricated all of these components using short sections of transmission line.
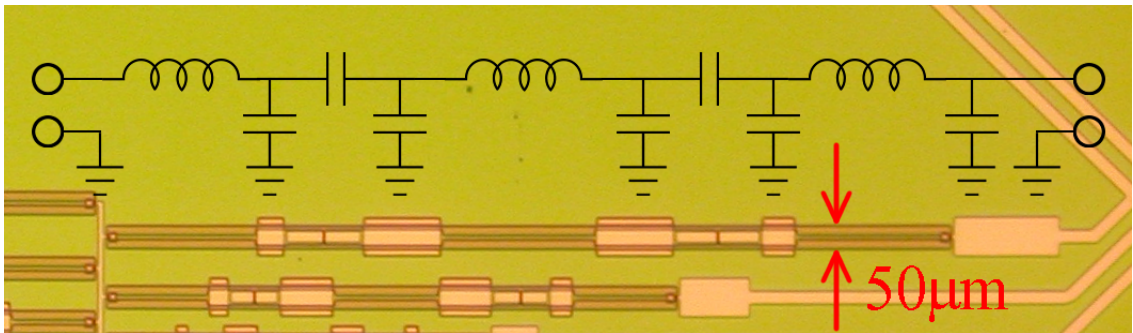


Figure 8.5. Photograph of a tubular filter in the channelizer with effective circuit drawn above. For scale, we labeled the total width of the CPW.
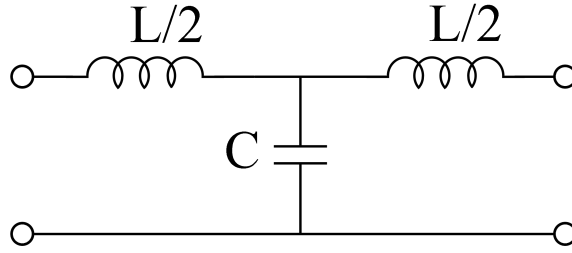
### 8.4.1  Short Transmission Lines



Figure 8.6. A T-network for a short transmission line

A short stretch of transmission line (shorter than $\lambda/8$) is equivalent to a tee-network with series inductance and shunt capacitance (See figure 8.6). The impedance matrix for this network is

$$Z_T = \begin{pmatrix} j\omega L/2 + 1/j\omega C & 1/j\omega C \\ 1/j\omega C & j\omega L/2 + 1/j\omega C \end{pmatrix} \tag{8.10}$$

The impedance matrix for the original transmission line with impedance $Z$ and length $\ell$ is

$$Z_{tline} = -jZ \begin{pmatrix} \cot(2\pi\ell/\lambda) \ \csc(2\pi\ell/\lambda) \\ \csc(2\pi\ell/\lambda) \ \cot(2\pi\ell/\lambda) \end{pmatrix} \tag{8.11}$$

Equating components between 8.10 and 8.11

$$L = \frac{2Z}{\omega} \left( \csc(2\pi\ell/\lambda) - \cot(2\pi\ell/\lambda) \right) \tag{8.12}$$

$$= \frac{2Z}{\omega} \tan(\pi\ell/\lambda) \tag{8.13}$$

$$\simeq Z\ell/v \tag{8.14}$$

where the last line only holds when $\ell \ll \lambda$ and where $v$ is the phase velocity. Similarly,

$$C \simeq Z^{-1}\ell/v \qquad (8.15)$$

A short but high impedance line will look like a series inductor while a low impedance line will look like a shunt capacitor (*Pozar* [2004]). These results are intuitive for microstrip: a wide low-impedance line looks like a parallel plate capacitor and will store energy in the electric fields between the conductors. Conversely, a narrow high-impedance line allows more energy to be stored in the magnetic fields circulating the upper conductor, boosting the line's inductance. The magnitude of both increase with the length of the section, but diverge from this simple model when $\ell$ becomes a significant fraction of a wavelength.

### 8.4.2 Trunk-line Inductors

In the operating band of the channelizer, the trunk-line inductors have reactances between 1.66 and 2.63 $\Omega$, which is much smaller than the bolometer terminations' normalizing impedance of 10 $\Omega$. We realized these inductors with 7 $\mu$m wide, 15 $\Omega$ microstrip lines that have lengths between 17 $\mu$m and 39 $\mu$m long.

### 8.4.3 Resonator Inductors

The resonator inductors are significantly larger than those in the trunk-line; at the band centers, the reactances are 41 $\Omega$. Even the thinnest and highest impedance microstrips that we can fabricate would be a significant fraction of a wavelength and would diverge from the model in Equation 8.14.

Coplanar waveguide (CPW) is an alternative transmission line that can have significantly higher impedance than microstrip. This higher impedance is achieved by splitting the ground plane into a wide slot and moving the upper-conductor down into the center of that slot, making it "coplanar." Since the ground can be moved significantly farther away from the center-conductor than in microstrip, the shunt-capacitance per unit length can be

much lower and the impedance higher. At the same time, removing the ground-plane in the vicinity of the line provides more space for the magnetic fields to build up, enhancing the inductance. Electrical currents in the center conductor are mirrored by half-magnitude return currents in the ground on each side of the slot. Equivalently, the slots conduct magnetic currents on each side of the center conductor with equal magnitude but opposite direction. This design has already been used by other researchers in the field; Caltech/JPL has used CPW for quasi-lumped inductance in several of their on-chip filter designs, including all of their antenna-coupled TES bolometers (*Goldin et al.* [2002] and *Chattopadhyay et al.* [2007])

Our CPW has a center conductor 10 $\mu$m wide, separated from the ground by 20 $\mu$m on each side, so they can be repeatably fabricated. They have 0.5 $\mu$m $SiO_2$ above, and 1 $\mu$m LSN plus $\sim$8 mm Si below. This geometry simulates in Sonnet to have an impedance of 82 $\Omega$, so the inductors that ranged between 30 and 94 pH had lengths between 44 $\mu$m and 141 $\mu$m, all less than $\lambda/8$. Like the microstrip, all simulations assumed a penetration depth into the Nb of 1000 *AA* (*Kerr* [1999]).

The inductors in the outside resonators of each filter must transition to microstrip so they can interface with the trunkline and bolometers. We implemented this with a standard microstrip-to-CPW transition where the opposing slots magnetically short. The microstrip's upper conductor crosses this slot and shorts to the center conductors through a superconducting via(*Simons* [2001]). The transition creates parasitic capacitance that we compensated for by shortening the end inductors.

### 8.4.4   Capacitive Pi-networks

The lumped series capacitors are actually a pair of identical capacitors in series. We formed them across 2 $\mu$m gaps in the CPW's center-conductor that were covered by an additional plate above the 0.5 $\mu$m $SiO_2$. This design made each of the two capacitors larger than a single one and hence more robust against over-etching. The series design also makes the total capacitance more robust against alignment errors. A shift of one Nb layer relative

to the other parallel to the propagation direction will reduce one of the capacitors while simultaneously increasing the other, compensating for the shift. We also made the lower conductor wider than the upper one to make the capacitor more tolerant against alignment errors transverse to the propagation direction.

Discontinuities in CPW can excite an unwanted even mode that has no current on the center conductor and oppositely oriented current on the two ground-planes. This current pattern is similar to those around a slot dipole antenna and *can radiate* ((*Simons* [2001])). Engineers often suppress this with a bridge that shorts the two grounds, forcing them to be equipotential. We surrounded the series capacitors with bridges, but made them and the center-conductor below wider to simultaneously provide the two shunt capacitors in the pi-network. To tune the pi-networks (e.g. for the first network in Figure 8.4(c)), we varied the lengths of both shunt and series capacitors in a Sonnet optimization such that:

$$|Y_{12}| \rightarrow \omega C_b$$

$$|Y_{11} - Y_{12}| \rightarrow \omega C_a$$

$$|Y_{22} - Y_{12}| \rightarrow \omega C_c$$

Optimizing with these goals compensates for parasitic capacitance in each of the three individual capacitors by modifying the other two.

### 8.4.5 Matching shunt capacitors

We matched the filters' normalized impedance (7 $\Omega$) to the 10 $\Omega$ output transmission lines with a large shut capacitor realized with a wide section of microstrip as per Equation 8.15 (*Pozar* [2004]). This component is far-larger than our $1\mu$m resolution limit and is robust against all over-etch and alignment concerns. We loaded the input port from the antenna with a similar microstrip shunt capacitor.

Figure 8.7 shows an ADS simulation of the entire microwave circuit. Original optimization of the ideal lumped components resulted in $S_{11} < -15dB$ across the band, but
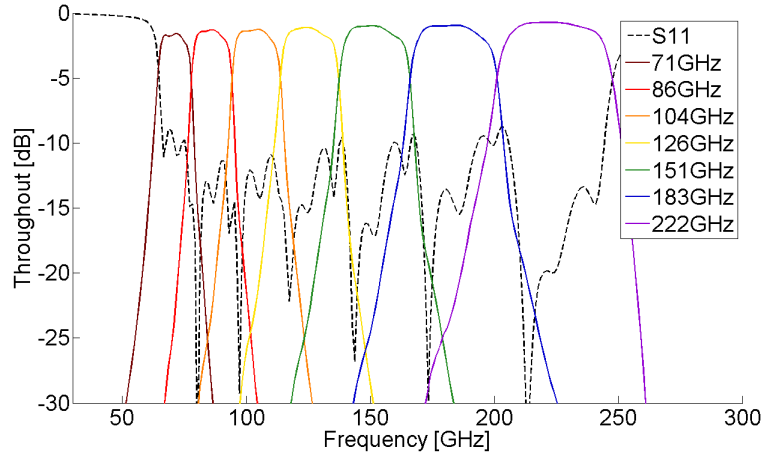
Figure 8.7. Channelizer scattering parameters simulated in ADS

the physical components have degraded this slightly by causing $S_{11}$ to rise to nearly -10dB between bands. The lowest channel also suffers from greater reflection.

## 8.5 Measurements of a sinuous antenna coupled to TES bolometers through a cochlea circuit
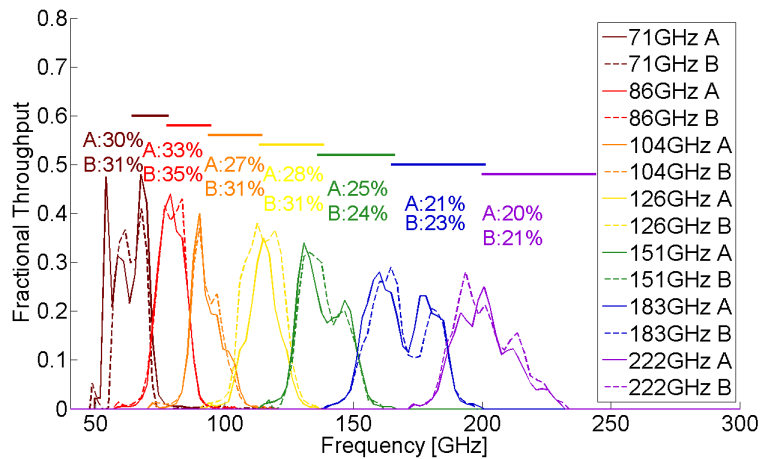


Figure 8.8. Cochlear Spectra measured with an FTS. Solid and dashed lines are the two polarization while the solid line above denotes the -3dB bandwidth. The band-averaged fractional throughputs are printed above the spectra.

Figure 8.1 shows the entire microwave structure. Each polarization from the antenna couples to the bolometers through a channelizer. We performed the same set of tests on this device as those in in chapters 6 and 7. As in chapter 7, we installed a 0.125 inch thick attenuator and Table 8.4 shows the measured attenuation for our system.

Figure 8.8 shows the normalized spectra, with the designed -3dB bandwidths depicted above. These pass-bands are 10% lower than expected, which we attribute to the oxide permittivity being a $\epsilon_r = 4.4$ instead of 3.8. In contrast to the diplexers and triplexers, we made no attempt to correct for spectral shifts since we had little prior experience with these filters.

While the inductance in the filters comes predominantly from magnetic fields, the inductance in the trunkline is from a mixture of magnetic and kinetic conductance. In simulation, the unexpected change in the oxide permittivity detunes the trunkline inductors, increasing the reflections off the channelizer input to and average of 8.4% accross all bands. For comparison, a correctly tuned channelizer should only reflect 2-3%. In Table 8.3, we show the loss from each optical component in the system and demonstrate that the total expected throughput is comparable to the measured values. After adding an AR coating to the lens and retuning the channelizer, we expect the receiver throughputs to increase to 30%-40%.

Table 8.3. Losses in the Channelizer Throughput

| Component | Power Transmitted |
|---|---|
| Optical Filters | $\approx$70% |
| Lens-vacuum interface | 72% |
| Antenna Front-lobe | 91% |
| Antenna-microstrip interface | 88% |
| Dielectric Loss | 70-90% |
| 1-$S_{11}$ channelizer | 91% |
| **Total** | 22-30% |

Figure 8.9 shows the measured beam patterns compared to simulation. These measurements were imperfect because the 3-layer coated lens de-laminated before this test and damage to the press precluded replacing it. As of the writing of this thesis, a lens has not been repaired with a working multi-layer coating and all tests of the cochlear channelizer used a bare lens. As a result of the missing coating the cross-polarized leakage was much

Table 8.4. Optical Power Transmission through MF110 with the Log-periodic Channelized device

| $f_{center}$ | Fractional Transmission |
|---|---|
| 80 | 63% |
| 97 | 49% |
| 117 | 36% |
| 140 | 31% |
| 170 | 24% |
| 207 | 16% |

higher and the throughput was lower than expected. However, we expect that these will improve with a properly coated lens. Nonetheless, there are significant asymmetries in the beams that suggest the antenna is not radiating in the intended modes as it did in the single channel differentially-fed devices of chapter 6. We suspect this occurred because the currents on the antenna were not properly balanced. While the lens can smooth power asymmetries in the beam, it can still generate non-circular beams when excited with a phase that is not circularly symmetric about boresight. In fact, we can use the script from chapter 4 to produce beams with qualitatively similar features as those measured in 8.9. We will likely correct these issues by feeding the antenna with a balun.

## 8.6 A simultaneous measurement of oxide permittivity and surface inductance

The filters in chapters 6 and 7 resonate at frequencies where the shorted stubs and inverters are $\lambda/4$. This resonance is set by the physical length of the lines and the wavespeed in those lines, which is a function of the oxide permittivity (through the capacitance per length) and the Niobium surface impedance (through the inductance per length; $v = 1/(c\sqrt{CL})$). The inductance is a mixture of magnetic and kinetic and as we argued in chapter 6, the kinetic makes a significant contribution because the line impedance is so low.

By contrast, the filters in this chapter resonate at frequencies set by the inductance and capacitance of *short* stretches of transmission line. Once again, the oxide permittivity influences the resonance through the capacitors. However, the inductance from the $82\Omega$
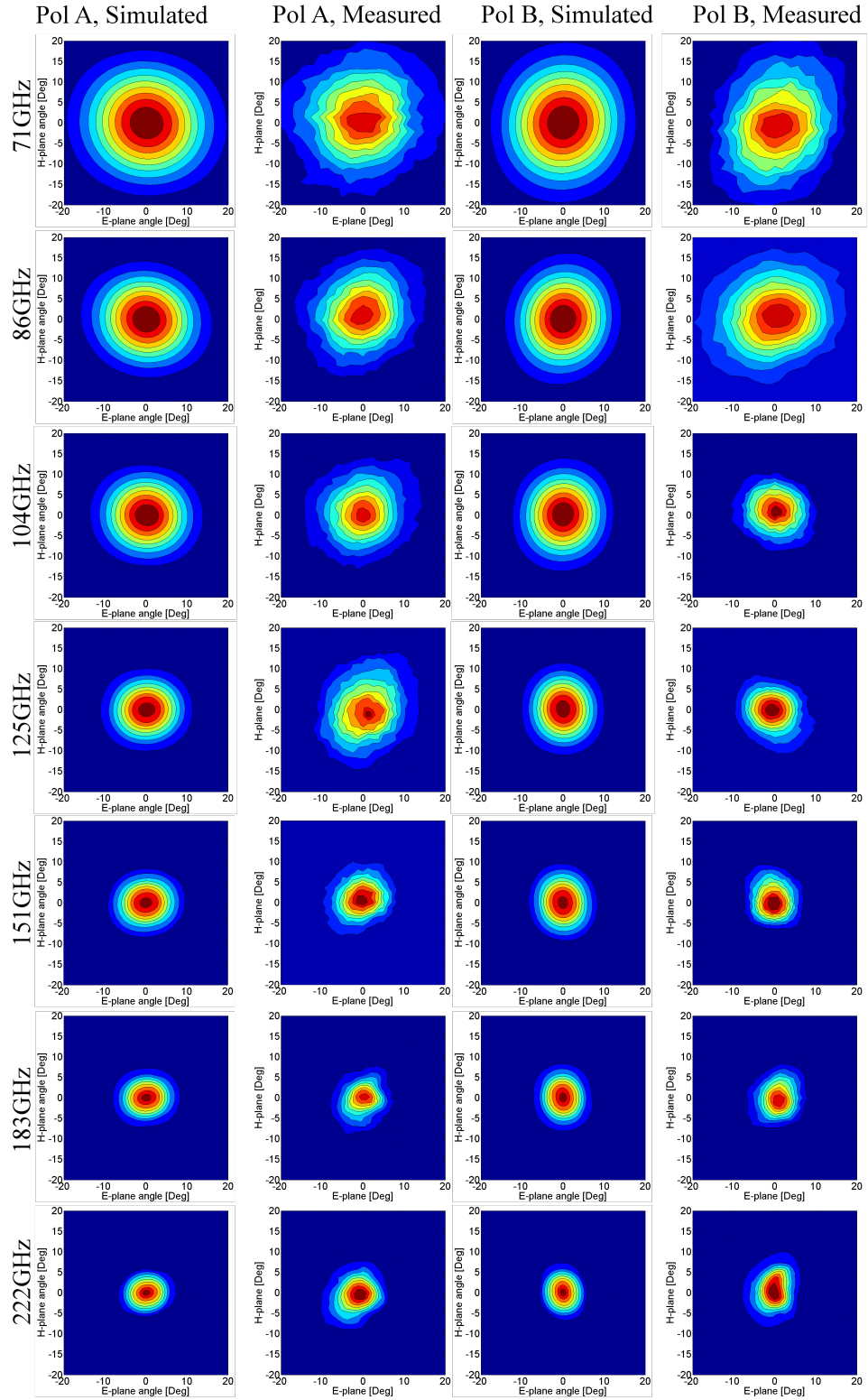
Figure 8.9. Simulations and measurements of sinuous beams through the channelizer.

CPW is almost entirely magnetic; kinetic inductance is subdominant. Because these two filters' resonances are presumably set by different combinations of $\epsilon_r$ and $L_s$, in principle, we can use data from the two filters to simultaneously constrain both material properties; we can break the degeneracy between material properties present in single filter measurements.

We simulated the filters' throughput $S_{21}$ in Sonnet while sweeping $\epsilon_r$ from 3.0 to 7.0 and $L_s$ from 0.06 to 0.26 pH/sq. For each parameter combination, we computed an *unnormalized* $\chi^2$ between measured and simulated data. We emphasize that we only simulated the individual filters and not the entire channelizer or Diplexer structures for computational ease. In practice, the entire circuit narrow the pass-bands and full simulations that reflect this effect would provide tighter constraints on $(\epsilon_r, L_s)$. Because these relevant systematic effects that are not reflected by the simulations, we have not bothered to normalize the $\chi^2$ values and so the absolute magnitude does not indicate confidence; only the best fit values can be inferred.

Figure 8.10(a) shows the *chi*$^2$ for different models $(\epsilon_r, L_s)$ in the distributed filter from chapters 6 and 7. The contours slope across the plot because the transmission-line wave-speeds depend on a combination of the two material properties. Figure 8.10(b) shows the same plot for the quasi-lumped filters from the log-periodic channelizer and it's contours clearly depends on a different combination of the parameters. The band-positions is only a weak function of $L_s$ because of the CPW's strong magnetic inductance. Finally, Figure 8.10(c) shows the sum of the two plots, indicating that $\epsilon_r = 4.4$ and $L_s = 0.18$ pH/sq. Figure 8.11 shows the co-plotted fits on the two filter data sets.

It is surprising that the surface inductance appears to be so high. Were it a lower but more expected value of 0.1 pH/sq, the two $\chi^2$ curves from the different measurements would intercept at a larger angle and provide a tighter constraint on the material properties. This large inductance suggests a penetration depth that is comparable to the film thicknesses. A more complete model (*Kerr* [1999]) for the surface impedance than Equation 6.2 is

$$Z_s = j\omega\mu\lambda \frac{(\eta + j\omega\mu\lambda)e^{t/\lambda} + (\eta - j\omega\mu\lambda)e^{-t/\lambda}}{(\eta + j\omega\mu\lambda)e^{t/\lambda} - (\eta - j\omega\mu\lambda)e^{-t/\lambda}} \qquad (8.16)$$
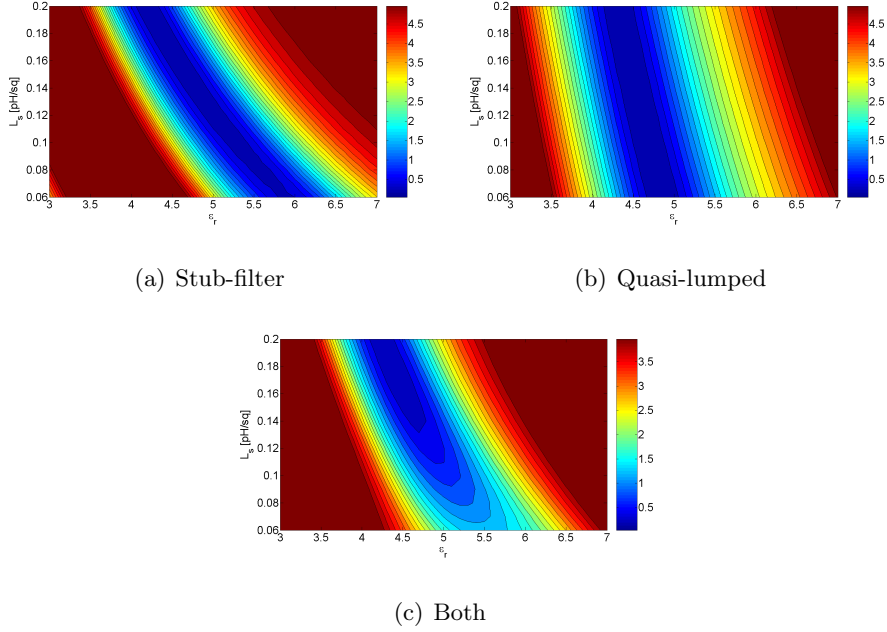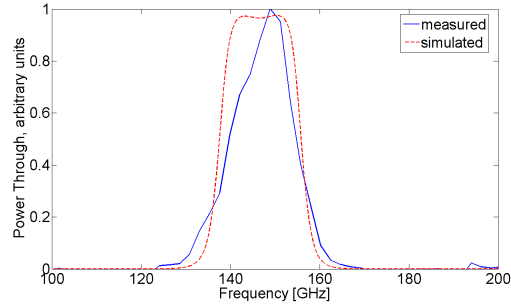
(a) Stub-filter            (b) Quasi-lumped

(c) Both

Figure 8.10. Un-normalized $\chi^2$ between measured bands at 150GHz and simulations with different values of oxide $\epsilon_r$ and Niobium $L_s$. The data show a preference for $\epsilon_r = 4.4$ and $L_s = 0.18$ pH/sq

where $\eta$ is the impedance of free space and $t$ is the Niobium film thickness. Inverting Equation 8.16 shows that our Niobium films have a penetration depth close to 0.24 $\mu$m, which is nearly as large as the ground plane thickness of 0.3 $\mu$m. Such a high penetration depth compromises the superconductor and could be responsible for some of the excess loss we have seen in our devices at higher frequencies.

The most significant source of systematic error in this analysis is our poor understanding of the oxide film thickness. While it is nominally 0.5 $\mu$m thick, we originally deposit 0.57 $\mu$m oxide expecting the Ar sputter etch that we use to remove Nb-oxide in the vias to also remove 0.07 $\mu$m. However, the oxide etch rate of this step is poorly characterized and could explain the deviations from traditional measurements that we see in our inferred material properties. For example, a reasonable 9% over-etch of the oxide film with the sputter etch would bias our permittivity result from 4.0 to 4.4. More work needs to be done to characterize this step.

This unexpected shift in material properties changes the microstrip-based trunkline

159

(a) Best fit Stubs
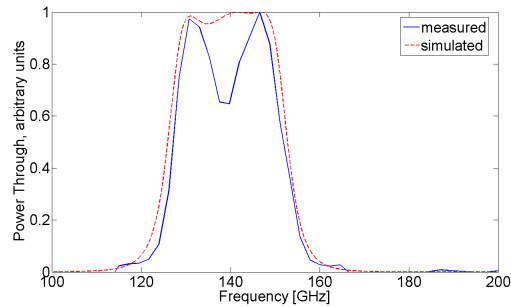


(b) Best fit Quasi-lumped

Figure 8.11. Best fit models co-plotted worth the two types of filter. Recall that we adjusted the stub filter in the diplexers and triplexers (this one's from the 90-150 Diplexer) to retune the center band while we made no such adjustments to the channelizer filters.

inductors in a different way than the CPW-based resonator inductors. As a result the entire circuit is de-tuned and simulating the channelizer with the new values suggests a reflection of $S_{11} \approx 16\%$. This helps explain the total throughput in our measurements and also suggests that we can re-claim this by re-tuning the channelizer with the new material properties. The throughput losses are summarized in Table 8.5

## 8.7    Conclusions

In this chapter, we summarized the design cochela-inspired methodology for channelizers that our UCSD collaborators have developed and also discussed how this can be realized in monolithic printed circuits needed for millimeter and sub-millimeter applications. The measurements are encouraging, showing high optical throughput in the expected frequency channels and beam patterns that are consistent with diplexer and triplexer devices. How-

Table 8.5. Losses in the Channelizer Throughput measurements

| Source | Power Transmitted |
| --- | --- |
| Optical Filters | $\approx$70% |
| Alumina-vacuum Lens surface | 72% |
| Antenna Front-lone | 91% |
| Antenna-Microstrip interface | 88% |
| Transmission line loss ($\tan(\delta) = 0.008$) | 70-90% |
| $1 - S_{11}$ of Channelizer | 84% |
| Total | 22-34% |

ever, the measurements should be repeated with a properly coated lens to demonstrate higher throughput and lower cross-pol contamination.

As mentioned in chapter 7, we can likely improve the beam shape with a different feeding scheme, and we discuss this in the concluding chapter.

There is one obvious modification that would improve the microwave design. Because the CPW 10 $\mu$m slot width is much larger than the 0.5 $\mu$m SiO$_2$ film thickness, it is not important that the center conductor be coplanar; it could just as well be in the layer above the oxide. In this case, the shunt-capacitor bridges would cross under the center conductor, as would the second plate for the series capacitor, residing in the ground plane. The merits of this design are that (1) the capacitors are completely robust against transverse alignment errors between the two Nb layers (although the inductor is not) and (2) no vias are required in the channelizer (although they are still needed at the antenna feed point). As of the writing of this thesis, we have not implemented this re-design.